Magnetic Resonance Imaging 61 (2019) 196–206

Contents lists available at ScienceDirect

Magnetic Resonance Imaging

journal homepage: www.elsevier.com/locate/mri

Original contribution

Distributions of discrete spherical particles with a constant susceptibility can lead to echo time dependent phase shifts which deviate from theories

Paul Kokeny[a], Yu-Chung N. Cheng[b,*], He Xie[c]

[a] Department of Biomedical Engineering, Wayne State University, United States of America
[b] Department of Radiology, Wayne State University, United States of America
[c] Department of Physics, Wayne State University, United States of America

ARTICLE INFO

Keywords:
Simulation
Static Dephasing regime
Lorentz sphere
MRI
Susceptibility

ABSTRACT

Purpose: When an object contains a distribution of discrete magnetic inclusions with a constant susceptibility, the MRI signal inside the object may no longer be determined analytically by assuming that the object is uniform or magnetic inclusions are completely random. Through simulations and experiments with spherical particles inside cylinders, this work is to study the signal behavior in the static dephasing regime.

Methods: MRI complex images of long cylinders containing spherical particles with different arrangements were simulated and compared to similar experimental phantom data. All experiments were designed for the static dephasing regime so that diffusion was neglected.

Results: Several factors can lead to different phase shifts over echo time. These include numbers of particles per image voxel, particle arrangements, and Gibbs ringing effects. Purely random arrangements of particles in simulations can agree with a revised theoretical formula at short echo times, but quasi-random arrangements of particles do not agree with the theory. In addition, close to half of experimental results show deviations from the theory and the quasi-random arrangements of particles can explain those experimental results. Simulated R_2' values are about the same for different cylinder orientations but increase when random particle arrangement is restricted toward lattice. Nonetheless, as expected, phase distributions outside and far away from each cylinder are independent of any factor affecting phase inside and behave as if they are from a cylinder with a uniform bulk susceptibility.

Conclusion: Phase over echo time inside an object containing discrete spheres can be nonlinear and deviate from current theories in the static dephasing regime. Phase outside the object can be used to accurately determine its magnetic moment and bulk susceptibility without a priori knowledge of the spherical particle distribution inside the object. These results can be extended to the subcortical gray matter and suggest that in vivo susceptibility quantification will need to be re-thought.

1. Introduction

Phase and magnitude information from magnetic resonance imaging (MRI) can be used for both the visualization and quantification of magnetic susceptibility. This is important clinically as the susceptibility of biological tissue is directly related to iron content or other sources such as calcium. Iron content in the brain is of interest as it has been associated with several diseases [1]. Quantitative susceptibility mapping (QSM) has also been an active research topic [2,3].

In most applications, an object or a tissue consists of numerous discrete magnetic inclusions rather than a purely uniform continuous medium. While induced magnetic fields from all these inclusions should be used to calculate the complex MRI signal behavior of the object, due to the current computational limitations, it has been convenient to treat the object as a continuous medium, especially for calculations of MRI phase values. However, it has been shown that the phase signal from the white matter does not agree with the model from a uniform medium, due to the microstructure such as axons in the white matter [4-6].

From a different consideration in physics, magnetic field calculations from a uniform macroscopic object can be separated into a far-field and a near-field contribution. The far-field contribution can be calculated from the geometry of the object with a uniform susceptibility [7]. The same calculation applies to the field distribution outside the object. The near-field contribution is zero for a continuous medium with an isotropic susceptibility and is taken into account by the Lorentz

* Corresponding author.
E-mail address: yxc16@wayne.edu (Y.-C.N. Cheng).

https://doi.org/10.1016/j.mri.2019.05.006
Received 24 February 2019; Received in revised form 17 April 2019; Accepted 4 May 2019

sphere correction. On the other hand, if the object is made up of discrete spherical inclusions, there is another near-field component that arises from the inclusions themselves, in addition to the Lorentz sphere correction. This additional near-field is also zero if the fast diffusion condition is met [8,9]. However, in the static dephasing regime where diffusion is neglected, the additional near-field contribution is not zero, as shown from nuclei magnetic resonance (NMR) frequency shifts in [8] with a theoretical background described in [10].

As the frequency shift in NMR due to the additional near-field contribution (Eq.(1) below) interpreted by [8] would imply that phase is linearly proportional to echo time (i.e., echo-time independent phase coefficient), while our previous simulations of particles in cubes [11] have shown echo-time dependent phase values from MRI, which completely disagree with Eq.(1), this major discrepancy requires further investigations. First, because Eq.(1) was derived under a general condition [10], as long as the volume fraction of particles in a system is less than 20% (according to [8]) but not super low, simulations from Ruh et al. [8] have shown perfect matches with Eq.(1). Thus, as NMR experiments use cylindrical tubes, the discrepancy may or may not disappear if we simulate discrete particles in cylinders rather than in cubes in [11]. If only a few particles are in a cylinder, their induced magnetic field distributions will highly depend on the location of each particle and simulated results will not match with the theory given by [10]. On the opposite side, if each particle is a point and the cylinder is completely filled by the points, then the cylinder is a continuous medium and its phase is described by Eq.(2) below. Thus, when a cylinder is filled with a sufficient number of particles, and when its magnitude intensity appears uniform, we want to study, first, the agreements between simulations and theoretical equations (Eq.(2) or Eq.(3) below). Second, under what conditions, the discrepancy between simulations and theories will appear. Third, whether these simulation results will somehow explain some nanoparticle experimental data in our previous work [12]. In addition, if we use a different material (i.e., polystyrene) for the experiments, whether the results will be similar. Finally, whether we learn anything new from all these results, whose conditions are all in the pure static dephasing regime.

In this work, the main goals are to (1) simulate gradient echo MR images from Fe_3O_4 nanoparticle solutions and from mixtures of polystyrene beads in gel, (2) analyze how several factors (the number of particles per voxel, the arrangement of particles, Gibbs ringing, etc.) from simulations can affect phase values, and (3) compare results between simulations, experimental data (nanoparticles and beads), and current theories (Eq.(2) and Eq.(3) below). In the Methods section, we start by briefing some theoretical background and equations that are relevant to our study here. Next, the experimental procedures of preparing and imaging Fe_3O_4 nanoparticle solutions and polystyrene beads are described in detail. Afterwards, general simulation procedures including the generation of fields and final images are described, followed by specific details for each material, due to different experimental setups. For polystyrene beads, we have to enhance the susceptibility effect from them and we try to match our simulation parameters with experimental parameters. For nanoparticle solutions, as it is not possible to match simulations with experimental parameters, we try to use roughly the same particle susceptibility in simulations for different solutions. The choices of those parameters have been validated in cubes [11]. In the fourth subsection under Methods, we describe the analyses of magnitude and phase images from each experimental and simulated data. The descriptions include careful procedures of removing the background phase. In the Results section, we compare simulated and experimental results to Eqs.(2) and Eq.(3). Deviations are observed. Lastly, implications of our results to practical brain imaging, particle distributions, and susceptibility quantification are discussed.

2. Methods

2.1. Background

The analytical work done by [10] on randomly distributed spherical particles within a large sphere has predicted a first-order frequency shift $\Delta\omega$ in the static dephasing regime at effectively infinite time.

$$\Delta\omega = -0.053\,\gamma\,B_0\,\lambda\,\Delta\chi \tag{1}$$

where B_0 is the main field strength, λ is the volume fraction of particles, $\Delta\chi$ is the magnetic susceptibility of the particles relative to their surrounding, and γ is the gyromagnetic ratio of the hydrogen proton with a value of $2\pi \cdot 42.58$ rad/s/T. In NMR where cylindrical test tubes are used for containing discrete magnetic inclusions, Ruh et al. [8] has expected such a frequency shift in addition to the original NMR frequency shift. On the other hand, an infinitely long cylinder with a uniform magnetic susceptibility $\Delta\chi'$ has the following phase inside the cylinder.

$$\phi_{in} = \gamma\,B_0\,T_E\,\Delta\chi'\left[\frac{3\cos^2\theta - 1}{6}\right] \tag{2}$$

where T_E is the echo time and θ is the angle between the axis of the cylinder and the main field. The left-handed system is adopted for the sign convention used in Eq.(2).

In either phantom or in vivo studies, which involve numerous magnetic inclusions inside long cylinders, most work so far has modeled those long cylinders with uniform susceptibility values and used Eq.(2). That is appropriate for the fast diffusion regime [8]. However, for the static dephasing regime where diffusion is neglected, results from [8] have suggested the following phase value inside a cylinder consisting of numerous discrete spherical particles when $\lambda < 0.2$.

$$\phi_{in} = \gamma\,B_0\,T_E\,\lambda\,\Delta\chi\left[\frac{3\cos^2\theta - 1}{6} - 0.053\right] \tag{3}$$

where $\lambda\Delta\chi = \Delta\chi'$ is considered as the bulk susceptibility of the cylinder. The second term in Eq.(3) may act as a near-field contribution to the original phase term (i.e., the far-field contribution). One of our goals is to examine the validity of Eq.(3).

2.2. Experiments

2.2.1. Fe_3O_4 nanoparticles

In our previous work [12], we have prepared and imaged a phantom containing four different susceptibility values of nanoparticle solutions in plastic straws (0.29, 0.56, 1.11, and 2.20 ppm). Each straw had an inner radius of 2.98 ± 0.03 mm and an outer radius of 3.20 ± 0.03 mm. Images were acquired from an 11-echo susceptibility weighted imaging (SWI) sequence on a 3 T Siemens Verio machine with the straws perpendicular and parallel to the main field. The imaging parameters relevant to our simulation parameters provided later were: 1 mm isotropic resolution, 2.89 T actual main field, and T_E ranging from 5.68 ms to 29.58 ms in increments of 2.39 ms. The image matrix size was 256 × 256 with 64 slices. Data from the first echo time of 5.68 ms or the highest susceptibility were not used, as either the phase effect was too small to measure or the dephasing effect was too heavy to maintain the signal-to-noise ratios (SNR). All other data were re-used in this work.

2.2.2. Polystyrene beads

In addition to the existing nanoparticle data, we conducted an experiment using large 90 μm diameter polystyrene spherical beads (Polysciences, Inc.) and gel doped with Gd-DTPA (0.5 M Magnevist). This doped gel acted as a reference in terms of susceptibility, and was used to surround the straw and to mix with beads inside a plastic straw as well. In this experiment, three identical 7-oz plastic cups were used

in order to remove background phase and the susceptibility effect from the straw itself. Cup 1 consisted of a straw filled with polystyrene beads and doped gel, surrounded by doped gel. Cup 2 consisted of a straw filled with and surrounded by doped gel. Cup 3 only had doped gel. The phantom construction procedure is as follows.

A single straw with the same dimensions used in the nanoparticle experiment was cut in half and glued to the bottoms of Cups 1 and 2. Distilled water of 600 ml and Magnevist of 36 ml were mixed together and heated to roughly 40° C using a hot plate. At this point, 15 g of gelatin powder was added and the whole solution was mixed uniformly. This concentration should lead to a susceptibility relative to water of about 9.4 ppm according to the molar susceptibility of Gd-DTPA [13]. With a reported magnetic susceptibility for polystyrene relative to water of − 0.26 ppm [14], this would lead to a susceptibility difference of about − 9.66 ppm between polystyrene and the doped gel (However, later our results show this was not the case). Roughly 312,000 polystyrene beads (about 0.12 ml in total volume) was added to 3 ml of doped gel, resulting in a volume fraction of about 3.8%, and transferred to the straw in Cup 1. The straw was entirely filled by the mixture of beads with doped gel. This led to roughly 100 beads per mm^3 inside the straw. Another 3 ml of gel with no beads was transferred to the straw in Cup 2. The remaining doped gel solution was then poured into all three cups outside the straws, all to the same height. All three phantoms were then covered and placed in a refrigerator to solidify.

MRI imaging was performed on a Siemens 3T Verio system with a single loop 6 cm diameter eye coil. Shimming was set to the default values obtained from the quality assurance performed by the Siemens service engineer. Such a choice was based on our previous work [15]. In order to properly remove the background phase, it was important that all 3 cups were imaged in the exact location relative to both the main magnet and eye coil. To achieve this, we secured the eye coil to a fixed position relative to the patient table. This allowed for each cup to be placed directly into the eye coil where the increasing diameter of the cup allowed it to sit firmly with the coil half way up the cup. For the parallel orientation, only the reference cup (Cup 3) and Cup 1 were needed to be imaged. In this orientation, each cup was secured on its side and the eye coil was laid flat onto the cup's side.

The 3D SWI sequence was used for imaging, with a TR of 37 ms and 6 echo times from 8.19 ms to 31.79 ms in increments of 4.72 ms. The read bandwidth per pixel was 219 Hz. A 1 mm isotropic resolution was used and the total matrix size was 128 × 128 × 64. When the straw was perpendicular or parallel to the field, the imaging orientation was coronal or transverse, respectively. As T_1 of the high concentration Gd-DTPA was significantly shortened, a flip angle of 80° and 6 averages of images were used to help increase the SNR. The total scan time for each cup was 30 min and 20 s.

2.3. Simulation procedures

In each simulation, we calculate magnetic fields and MRI signals from a distribution of spherical particles inside a finite cylinder (which is shown in Fig. 1), centered within a 3D rectangular field of view (FOV). Each simulated case corresponds to beads or nanoparticles inside a straw used in experiments. We try to match as many simulation parameters to experimental values as possible. These include echo times, cylinder diameter, center of the cylinder at the sub-voxel location, magnitude signal ratio between inside and outside the cylinder (in order to match the Gibbs ringing), bulk susceptibility, and number of particles per voxel for polystyrene beads. However, as the actual volume fractions of nanoparticle solutions are very low, which leads to very large grid sizes that cannot be handled with current computer memory, higher volume fractions are used in our nanoparticle simulations. As we have found out from our previous work [11], as long as the bulk susceptibility and particle arrangement are the same, varying the volume fraction and particle susceptibility (in the range of 1 to 20 ppm) leads to the same phase shifts as a function of echo time. In the end, 4 different bulk susceptibilities (1 for polystyrene beads and 3 for nanoparticles) have been simulated at orientations both perpendicular and parallel to the main field. Each case has been re-simulated 2 or 16 times (depending on the numbers of particles in simulations) using different seed values for the random number generator, in order to reduce variations through averages of results.

The basis of our simulation procedures has been described in [11]. Briefly, the magnetic field distributions will be added from contributions of each individual spherical particle on a 3D high-resolution matrix. This process of addition is circumvented by the convolution of the 3D Green's function and the geometry of all particles. The high-resolution field data are then converted to phase values. A separate high-resolution spin density grid, in which the values inside particles are set to zero but set to unity outside them, is combined with phase values to form a high-resolution complex grid. The low-resolution magnitude and phase images are created through a Fourier transform of the high-resolution complex grid, a cropping in k-space (with its size described below), and an inverse Fourier transform of the cropped grid. Due to the large scales of these simulations, several modifications have to be made in order to conserve computer memory and computation time.

The first modification utilizes the far-field and near-field concept. Regions of particles far from a region of interest can be treated as a continuous medium. Based on this concept and the linear summation of magnetic fields, an infinitely long cylinder containing discrete particles can be decomposed to a combination of a short cylindrical section containing particles and an infinitely long cylinder filled by a continuous medium, with a subtraction of the same short section from the continuous medium. This is illustrated in Fig. 1. The field distributions calculated in the middle cross sectional plane of the cylinder will be analyzed.

The second modification takes advantage of the 3D even symmetry of the Green's function and of the finite cylinder in the rectangular FOV. As a cosine Fourier transform performed on one half of a function with even symmetry is equivalent to performing a fast Fourier transform on the entire function, the use of a cosine Fourier transform on one half of the FOV in all three dimensions saves a factor of 16 in computation time and memory [16]. However, as a result, the particles will only be randomly placed within one octant of the cylinder, and then reflected over other octants. This is shown in Fig. 2. Included in the saved computation time, the actual reflection process only needs to be performed after the high-resolution complex grid is cropped in k-space. A fast inverse Fourier transform is then applied to the reflected k-space data and the final low resolution images of the entire FOV including the cylinder are reconstructed.

Third, we tried to mimic the Gibbs ringing from experiments by measuring magnitude signals inside and outside each straw at every echo time, and then matching these values in simulations. The center of each straw in the experiment was obtained from the Complex Image Summation around a Spherical or a Cylindrical Object (CISSCO) method [17] with sub-voxel accuracy, which was also matched in simulations of cylinders by adding the appropriate linear phase in k-space, in order to create a sub-voxel shift in the spatial domain.

Three different particle placement methods were used: one for purely random particle arrangements, one for quasi-random particle arrangements, and a lattice arrangement. For the purely random arrangements, particles were first randomly placed throughout the entire high resolution grid, ensuring that no overlap of particles would occur. For the quasi-random arrangements, each particle was constrained to a volume of 34^3 grid points and allowed a random placement within a smaller cubic sub-volume. This idea was described in more detail in [11]. Cubic sub-volume sizes of 8^3, 14^3, and 26^3 were used. After all particles were placed, one octant of a cylinder was defined at the corner of the high resolution matrix and all particles outside this cylinder were removed. In a separate simulation, the exact same octant of the cylinder filled by a continuous medium was defined and was used to generate

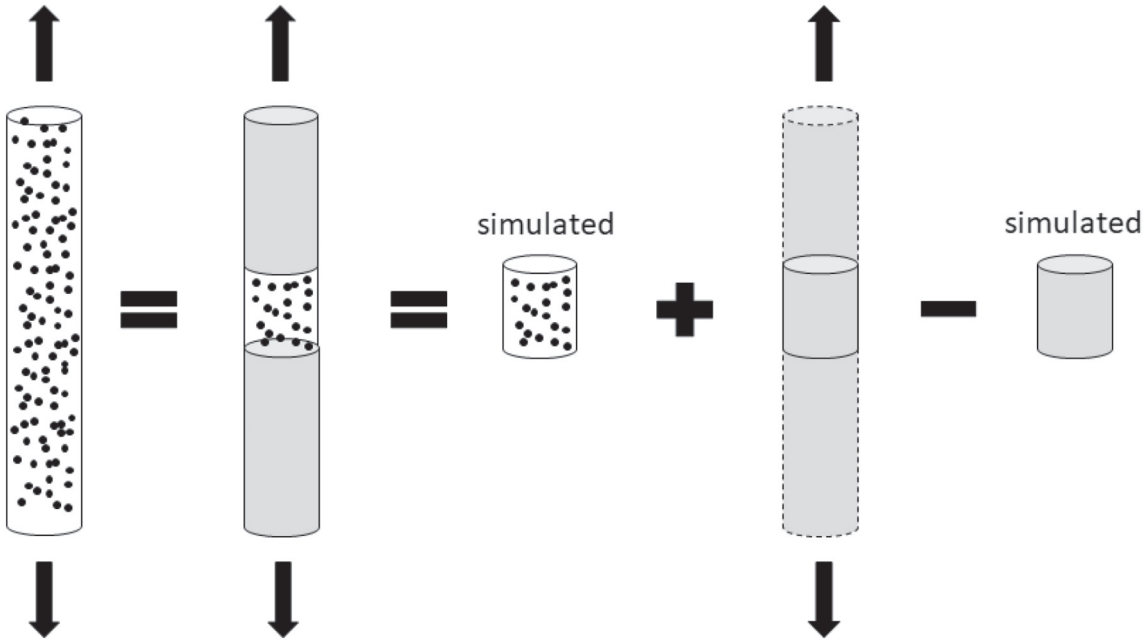

Fig. 1. A graphical illustration of the first modification made to our simulations. Regions far from the center of our finite cylinder can be treated as continuous mediums. The cylinder is modeled within a rectangular FOV, where all the fields and MRI signals are calculated for each grid point. This modification reduces the memory required for simulations as we only need to model the central finite section of an infinitely long cylinder.

field distributions as described above in the first modification.

In all simulations, the radius of each spherical particle was chosen to be 4 grid points in the high-resolution matrix [11] and this choice, carefully validated in [11], led to a volume of 257 grid points. The susceptibility value of each particle was set to be the desired bulk susceptibility of the cylinder (quantified from experimental data) divided by the volume fraction of the particles. The final low-resolution matrix size of the entire FOV was $16 \times 16 \times 40$ and the final short

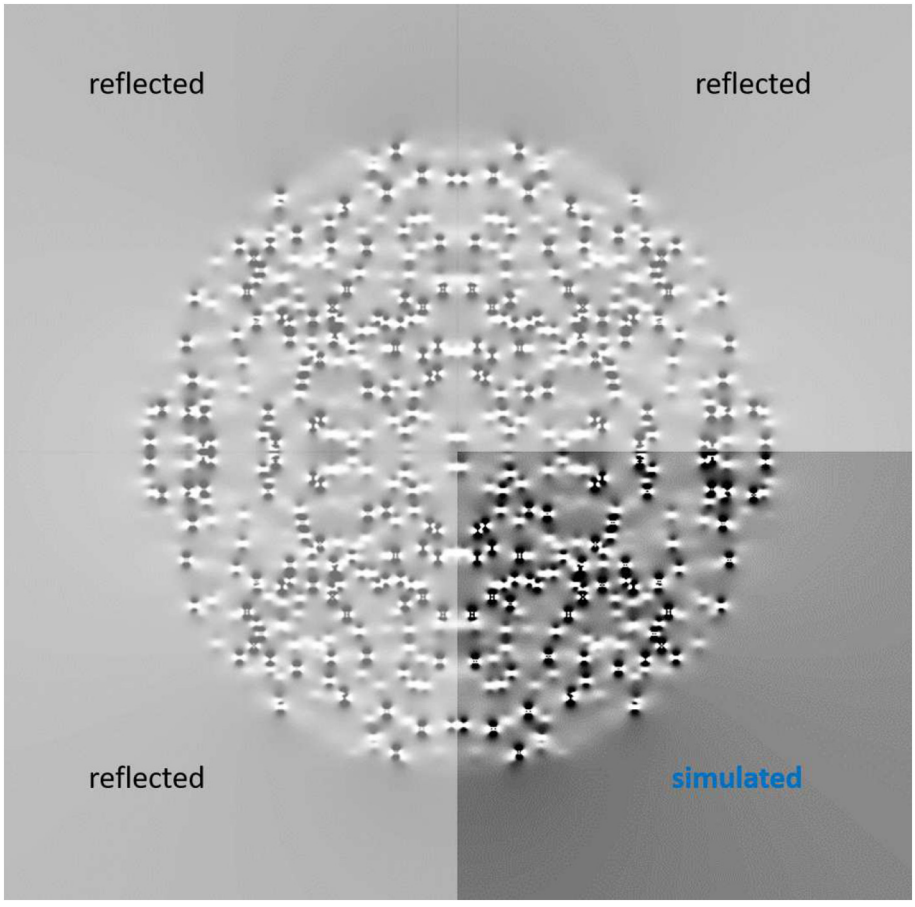

Fig. 2. A high-resolution cross-sectional phase image of the simulated cylinder containing randomly distributed spherical particles. This demonstrates the second modification made to our simulations. Only one octant of the cylinder is actually simulated and all other octants are later reflected in the low resolution. This modification reduces the memory and time required for simulations by a factor of 16.

cylinder had a radius of 3 pixels and a length of 20 slices. The size of the high-resolution matrix depended on the desired number of particles per voxel and their volume fractions, whose information are provided below. A main magnetic field of 2.89 T was used for all simulations, as this was the actual field strength of our Siemens 3 T Verio system. Echo times used in simulations were matched with their corresponding values in experiments.

Fortran was used to perform all simulations. A Linux based computing system centralized in our university was used. This computing system allowed for the use of up to 1.5 TB of RAM and utilized an Intel E5-2697v3 2.6 GHZ processor. The codes were made publically available on GitHub at https://github.com/pkokeny/DCT-Cylinder.

2.3.1. Other simulation details for Fe_3O_4 nanoparticles

The volume fractions needed to be lower than 20% so Eq.(3) would be valid [8]. All simulations for nanoparticle concentrations used 1728 particles per voxel. For particles randomly distributed inside cylinders, volume fractions of roughly 2.8%, 5.2%, and 11.8% were chosen for the bulk susceptibilities of 0.29, 0.56, and 1.11 ppm [12], respectively. These values led to relatively consistent particle susceptibilities of roughly 10.4 ppm, 10.8 ppm, and 9.4 ppm, respectively, which fell between 1 ppm and 20 ppm tested in [11]. The corresponding high-resolution grid sizes were $2016 \times 2016 \times 5040$, $1632 \times 1632 \times 4080$, and $1248 \times 1248 \times 3120$. With the respective crop factors of 252^3, 204^3, and 156^3 applied to the central portion of k-space, these high-resolution matrices were reduced to achieve the final $8 \times 8 \times 20$ low-resolution matrices (and $16 \times 16 \times 40$ after reflecting over each axis). Two different random particle arrangements were simulated and averaged for each bulk susceptibility and cylinder orientation, in order to improve the accuracy of the results. For the largest grid size, each arrangement took about 48 h to simulate results from all 10 echo times. A set of simulated images are shown in Fig. 3.

Only one quasi-random particle arrangement for the bulk susceptibility of 0.29 ppm with the cylinder perpendicular to the main field was simulated, as it was used to show a much better agreement with the experimental results than the purely random arrangement. This simulation used a high resolution grid size of $1904 \times 1904 \times 4760$ and a crop factor of 238^3, in order to satisfy a multiple of the 34^3 unit volume used in our quasi-random arrangements. The cubic sub-volume was 26^3 grid points. In this case, the resulting volume fraction was 3.3% and the particle susceptibility was about 8.8 ppm.

2.3.2. Other simulation details for polystyrene beads

All simulations for polystyrene beads used 125 particles per voxel. For particles randomly distributed inside cylinders, a volume fraction of roughly 3.7% and a particle susceptibility of roughly $-$ 6.5 ppm were used. These values led to a bulk susceptibility of roughly $-$ 0.24 ppm, measured from experiments using procedures described below. The high-resolution grid size was $760 \times 760 \times 1900$ and the crop factor was 95^3. For a separate set of simulations, all 3 cubic sub-volume sizes of quasi-random arrangements, lattice arrangement, and an additional randomly distributed arrangement with the 0.65% volume fraction were used for simulating polystyrene beads. For quasi-random arrangements, as each particle was allowed to move within a unit volume of 34^3 grid points, this led to a crop factor of 170^3, a volume fraction of roughly 0.65%, and a high-resolution grid size of $1360 \times 1360 \times 3400$. As a result, the particle susceptibility was roughly 37 ppm, which fell outside the range tested in [11]. In all these simulations, 16 arrangements were simulated and averaged for each cylinder orientation, in order to effectively get closer to the desired 1728 particles per voxel and improve the accuracy of our results.

2.4. Data analysis

For all experimental and simulated images, we would like to quantify the bulk susceptibility of each cylinder using only the phase outside, to check the SNR and determine the phase values inside the cylinder at each echo time, and to calculate R_2^*. Uncertainties were estimated using the error propagation method. Procedures of these tasks are described below.

2.4.1. Experimental data from Fe_3O_4 nanoparticles

Archived and processed complex images of nanoparticles in water from [12] were re-analyzed. Sixteen pixels of each slice over the 9 central slices inside the straw were averaged at each echo time for perpendicular and parallel orientations. The means and standard

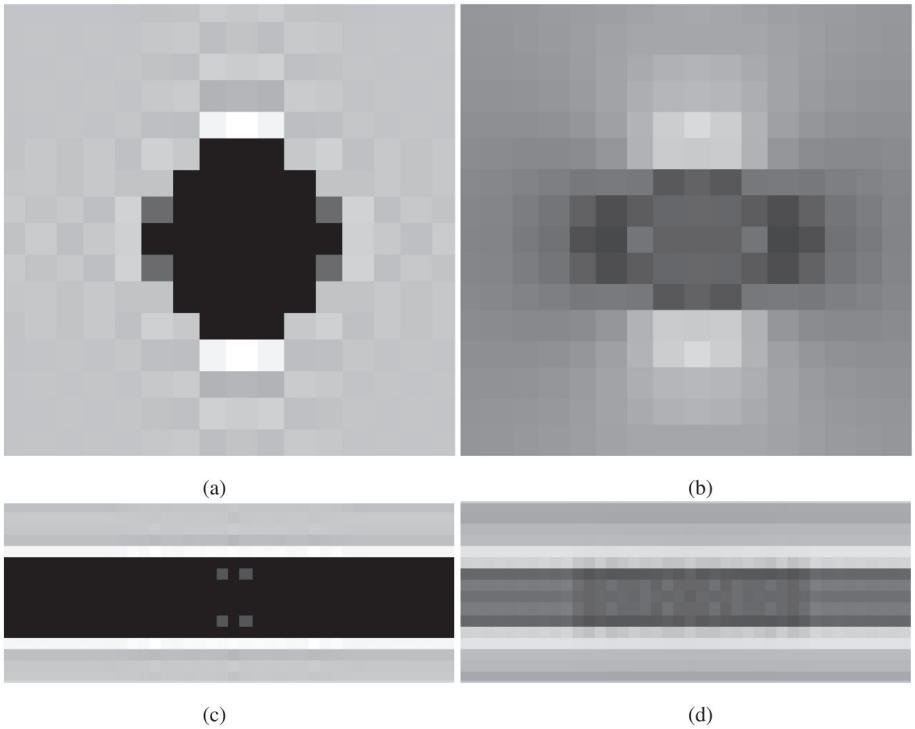

Fig. 3. Simulated images with a bulk susceptibility of 0.29 ppm intended for nanoparticles in an infinitely long cylinder perpendicular to the main field. (a) Magnitude and (b) phase image display the middle cross section (i.e., central slice) of the cylinder. (c) Magnitude and (d) phase image display the cross section parallel to the cylinder axis. The difference between the central finite section where individual particles are simulated versus the sections which are treated as continuous above and below the central section can be seen in (d).

Table 1
Bulk susceptibility $\Delta\chi'$ (in ppm) of each experimental and simulated cylinder. These values are calculated from the known cylinder (or straw) radius and the magnetic moments further quantified from the CISSCO method.

Fe_3O_4	Experiment	1.11 ± 0.02	0.56 ± 0.01	0.29 ± 0.03
	Simulations	1.08 ± 0.02	0.54 ± 0.01	0.28 ± 0.03
Polystyrene beads	Experiment	− 0.24 ± 0.03		
	Simulations	− 0.24 ± 0.01		

deviations (i.e., image noise) of both magnitude intensities and phase values were calculated from those 144 voxels, which also included Gibbs ringing effects. Thus, SNRs were estimated from magnitude images and each R_2^* was determined by performing linear regression on the natural log of magnitude intensities over three echo times from 8.07 ms to 12.85 ms. Phase data from any echo time with an SNR less than 3:1 from magnitude images were omitted from the results. With the known diameter of the straw, the CISSCO method was applied to processed phase images in order to determine the bulk susceptibility and sub-voxel center of each straw from the perpendicular orientation.

2.4.2. Experimental data from polystyrene beads

The phase distributions inside each cup but outside each straw were measured and symbolically expressed by:

$$\begin{aligned} \phi_{cup1} &= \phi_{bkg} + \phi_{straw} + \phi_{beads} \\ \phi_{cup2} &= \phi_{bkg} + \phi_{straw} \\ \phi_{cup3} &= \phi_{bkg} \end{aligned} \quad (4)$$

where ϕ_{bkg} was the background phase induced from eddy currents and the geometry of the cup itself. The induced phase ϕ_{straw} was due to the susceptibility difference between the straw wall and doped gel ($\Delta\chi_{straw-Gd}$). Similarly, ϕ_{beads} was the induced phase due to the susceptibility difference between each bead and the doped gel ($\Delta\chi_{bead-Gd}$).

The goals in this subsection were to quantify the correct phase inside the straw containing beads ($\phi_{in,beads}$) and to measure the bulk susceptibility of the beads relative to that of gel doped with Gd-DTPA, $\lambda_{beads}\Delta\chi_{bead-Gd}$, where λ_{beads} was the volume fraction of the beads. Ideally we could subtract ϕ_{cup2} from ϕ_{cup1} through a complex division, leaving only ϕ_{beads} and $\phi_{in,beads}$ in phase images. However, as the straw positions in Cups 1 and 2 did not match perfectly, the first required step was to remove ϕ_{bkg} from both ϕ_{cup1} and ϕ_{cup2} through complex divisions with ϕ_{cup3}. After each complex division, a constant background phase still remained in each set of phase images, ϕ_{cup1} and ϕ_{cup2}. This constant phase needed to be estimated and removed in order to obtain accurate measurements of ϕ_{beads} and $\phi_{in,beads}$. To achieve this, we had to first roughly estimate and remove ϕ_{straw} and $\phi_{straw} + \phi_{beads}$ from ϕ_{cup2} and ϕ_{cup1}, respectively, with the remaining phase assumed to be a constant. This was because around the straw ϕ_{straw} dominated the overall phase distributions and it prevented a good estimation of the constant phase. As the CISSCO method was insensitive to the additional constant background phase for a cylinder perpendicular to B_0 [17,18], we used CISSCO to quantify the effective magnetic moments and centers of the straws (with and without beads) from the central slice but average the values from all echo times. We used these information to forward simulate ϕ_{straw} and $\phi_{straw} + \phi_{beads}$. We then removed them from ϕ_{cup2} and ϕ_{cup1} through another set of complex divisions, respectively, and estimated the constant background phase in each set of images. After we removed the estimated constant background phase values from ϕ_{cup2} and ϕ_{cup1}, this resulted in more accurate phase distributions inside and outside the straws. From there, the effective magnetic moments of both straws (from Cups 1 and 2) were re-quantified. The difference of these two effective magnetic moments led to the effective magnetic moment of the cylindrical gel containing beads. Given the known inner radius of the straw, this effective magnetic moment allowed us to directly calculate $\lambda_{beads}\Delta\chi_{bead-Gd}$. On the other hand, as the straw had no effect on the phase inside, after removing the constant background phase, we directly measured the remaining phase inside the straw containing beads ($\phi_{in,beads}$) from ϕ_{cup1}. For the straw parallel to B_0, as $\phi_{straw} = \phi_{beads} = 0$ outside the straw, the constant background phase was directly measured and removed from complex divided images between Cups 1 and 3, i.e., $-i\ln(\exp(i\phi_{cup1})/\exp(i\phi_{cup3}))$.

Given the low number of particles per voxel, it was important to average the phase over many voxels inside the straw for analysis. The same process to analyze the nanoparticle magnitude and phase data was used here, by averaging sixteen pixels from each slice over 9 central slices inside the straw. The R_2^* were determined from the first three echo time of the bead data.

2.4.3. Simulated data

Simulated images were analyzed in the same way as done for the above experimental data, except that sixteen pixels from each slice of only the central six slices were averaged. This choice was because the simulated images were more accurate for pixels closer to the central slice. Bulk susceptibilities, phase values inside straws, and relaxation rates were all compared between simulations and experiments.

3. Results

Bulk susceptibilities quantified from CISSCO are given in Table 1. These results between experiments and simulations are in very good agreements.

Figs. 4 and 5 show mean phase values inside straws from the experiments, simulations, and theoretical values from Eqs.(2) and(3). Data points from images at long echo times with an SNR less than 3:1 are not shown. Each error bar in these plots represents one standard error of the mean. In general, simulated results from randomly distributed particles agree with the formula given by Eq.(3), within two standard errors but mostly outside one standard error. However, some experimental data shown in Fig. 4a and Fig. 5c, or at long echo times in Figs. 4 and 5, do not agree with Eq.(3), for more than 3 standard errors. As we see from simulated results shown in Fig. 6, different particle arrangements inside a long cylinder can lead to nonlinear phase dependence of echo time. This nonlinear behavior appears more obvious when we further restrict the particle's freedom of movement toward a lattice arrangement. In the case shown in Fig. 4a, simulated results with the quasi-random arrangement using a cubic sub-volume of 26^3 grid points agree better with experimental data. This suggests that such a quasi-random arrangement may occur in that nanoparticle solution.

As demonstrated from three different voxels in Fig. 7, it is clear that Gibbs ringing over the cross sectional plane of a simulated cylinder shows a large effect from voxel to voxel. Thus, the simulated data must be averaged over a sufficient number of symmetric voxels inside a narrow cylinder. After averaging, those results shown in Figs. 4 and 5 are not affected by the Gibbs ringing effect. We have also independently verified this point, by simulating and comparing the phase from the middle pixel of a wider cylinder (which is minimally affected by the Gibbs ringing effect) to the averaged phase within the cylinder.

Table 2 shows R_2^* quantified from experiments and R_2' from corresponding simulations with random particle arrangements. The R_2^* values from nanoparticle experiments are in good agreements with original results from [12]. The R_2' values quantified from simulations agree with the theoretical $R_2' = 0.4\gamma B_0|\Delta\chi'|$ [10] within uncertainties, although each uncertainty of R_2' is quite large even when no thermal noise is included in simulations. Those R_2' values from simulations also agree with experimental data, except for the highest bulk susceptibility of the nanoparticle solution. The disagreement in that case has been explained in [12] and in short, is attributed to the use of non-optimal echo times for R_2' quantification. From Table 2, there appears to be no dependence of cylinder orientation on R_2^* from experiments or R_2' from simulations. In the quasi-random and lattice arrangements of particles in simulations, it is seen that R_2' increases as the particles become more

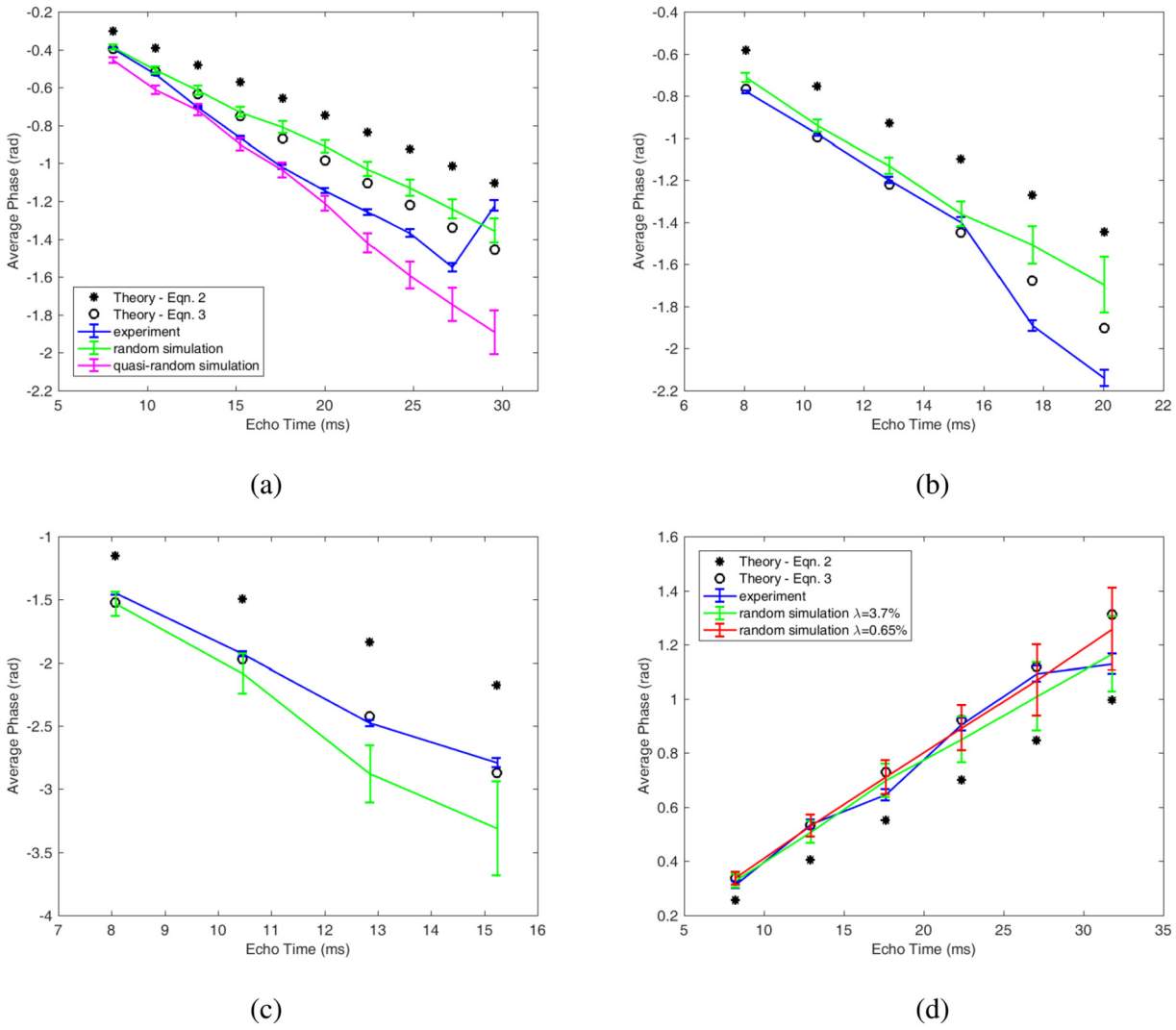

Fig. 4. Experimental and simulated results, as well as two theoretical predictions, of phase inside cylinders perpendicular to the field are shown for bulk susceptibilities of (a) 0.29 ppm, (b) 0.56 ppm, (c) 1.11 ppm, and (d) − 0.24 ppm. Panels (a), (b), and (c) show results from nanoparticle solutions, while panel (d) shows results from the beads mixed in gel. Asterisk markers represent the phase calculated from Eq. (2). Open circle markers represent phase calculated from Eq. (3). The blue lines represent the experimental data and the green lines represent simulated results using random particle arrangements. In (a), a quasi-random simulation is plotted in magenta with each particle allowed to move within a sub-volume of 26^3 grid points. These results seem to agree with the experimental data better. In (d), the green and the red line are from particle volume fractions of 3.7% and 0.65%, respectively, with the same bulk susceptibility. While both simulated results agree with the experimental data, the outcome from the volume fraction of 3.7% agrees better with the experimental data especially at the last echo time.

ordered, while the quantified bulk susceptibility from phase outside the cylinder is unaffected (Table 3). The former statement is in agreement with the results from [11].

Based on the quantified bulk susceptibility and known volume fraction, we estimated a susceptibility of roughly − 6.5 ppm for our beads relative to the doped gel, while its theoretical value was − 9.66 ppm. From the effective magnetic moment quantified from the straw wall relative to Gd-DTPA doped gel (i.e., Cup 2), the estimated $|\Delta\chi_{straw-Gd}|$ was 9.3 ppm, which agreed with the theoretical molar susceptibility from [13]. Thus, our numbers here showed that the susceptibility of our beads was not − 0.26 ppm relative to that of water, as given by [14]. In fact, the mass density of polystyrene beads should be about 1.05 g/cm^3, but we have found that the mass density of our beads is at least 1.2 g/cm^3, which indicates that our beads are not made of pure polystyrene.

4. Discussion

Our experimental and simulated results from a simple system do not completely agree with current theories applicable to the static dephasing regime (i.e., Eqs.(2) and(3)). Yablonskiy and Haacke [10] have considered spherical magnetic particles randomly distributed in a large space without a defined geometry. In other words, as long as spherical magnetic particles are randomly distributed in a large space with a low volume fraction, their theoretical formula, which gives a constant frequency shift shown in our Eq.(1), is what we should expect when the factor $|\delta\omega_s \cdot t|$, which is equal to the absolute phase value on the equator of the spherical particle, is much larger than 1. Ruh et al. [8] have further shown from simulations that Eq.(3) is valid in the static dephasing regime, as long as the volume fraction of spherical particles is less than 20%. However, all volume fractions in our work are less than 20% and we find disagreements between our results and theories. Looking closely, each of our simulated results from completely random arrangements of spheres in Fig. 4 at long echo times deviates further away from Eq.(3). At those echo times, the factor $|\delta\omega_s \cdot t|$ ranges from 17 to 27. From a pure theoretical point of view, the larger the factor $|\delta\omega_s \cdot t|$ is, the better the agreement between simulations and Eq.(3) should be. However that is not the case here. When we simulate phase

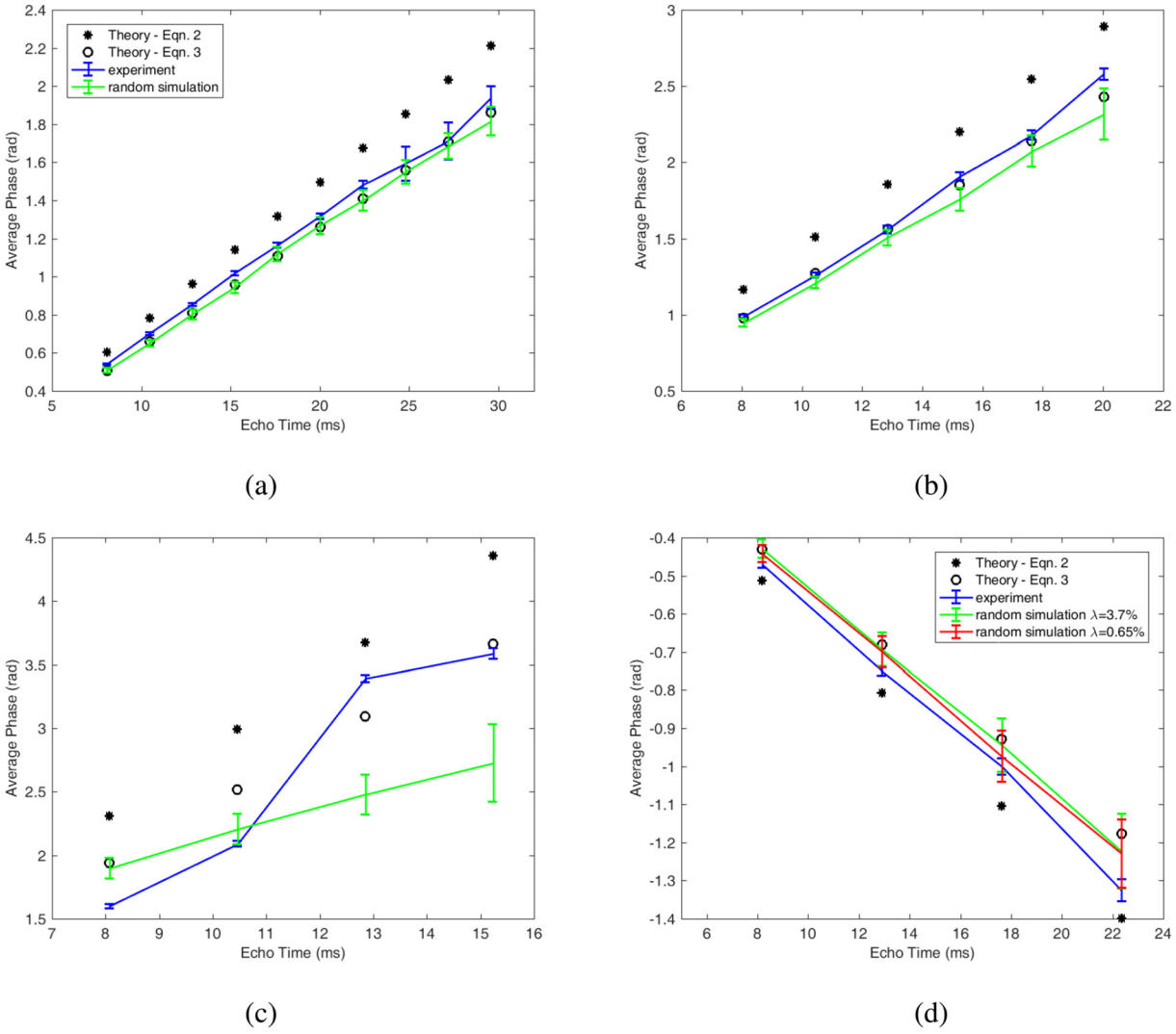

Fig. 5. Experimental and simulated results, as well as two theoretical predictions, of phase inside cylinders parallel to the field are shown for bulk susceptibilities of (a) 0.29 ppm, (b) 0.56 ppm, (c) 1.11 ppm, and (d) − 0.24 ppm. Again, panels (a), (b), and (c) show results from nanoparticle solutions, while panel (d) shows results from the beads mixed in gel. Meanings of the symbols and curves have been explained in the caption of Fig. 4.

values from echo times between 15 ms and 30 ms for the 1.11 ppm case, those results become very nonlinear and do not agree with Eq.(3) at all (see Fig. 8). The derivation of Eq.(1) is the first order expansion of the full equation in [10] and the full equation is also equivalent to the case of only a single particle residing at the center of a spherical volume. While our simulations also do not include the magnetic field interactions between particles, we do add up field contributions from each particle spread in the entire volume. As a result, our simulations should have included some near-field effects from neighboring particles, especially at longer echo times or higher particle volume fractions, but these effects are ignored in the theory.

Simulations from quasi-random arrangements of spheres do not agree with either Eq.(2) or Eq.(3). One example is shown in Fig. 4a (the magenta curve). As we have shown in Fig. 6, particle arrangements in a given medium can apparently affect phase values inside the medium and this is not predictable by any theory in advance. However, the experimental data shown in Fig. 4a agree better with the simulation from a quasi-random arrangement of spheres. A close check of our experimental results shows that close to half of them in Figs. 4 and 5 do not agree with Eq.(3) by more than two standard errors, over a range of echo times and different materials. All these results suggest that in experiments or reality, both quasi-random arrangements and completely random arrangements of particles can happen, but current theories only predict results from the completely random cases with neglected near-field effects, as theories were so derived. We also note from our data shown in Figs. 4 and 5 that those additional phase shifts at each echo time seem to be independent of the orientation of the cylinders. See our previous analysis shown in [12].

Our results may be used to explain the additional phase shifts shown by [19,20] in the subcortical gray matter in the basal ganglia, whose major susceptibility source is ferritin. If we reduce the particle susceptibility to 1 ppm in Fig. 4a, patterns of simulated curves will still be similar but the bulk susceptibility of the solution will be roughly 0.03 ppm. Thus, the potential of using simulations to explain current in vivo observations is there. In past work such as [21], microstructures such as cylinders representing axons in the white matter lead to nonlinear phase shifts. The recent trend is to use Generalized Lorentzian approach [21], susceptibility anisotropy [22,23], or ellipsoidal microstructures [24,25] to explain the phenomena. The focus has been white matter, not gray matter. Rudko et al. [26] have shown additional phase shifts from the cortical gray matter, but that situation mimics myelin in the white matter. Schweser and Zivadinov [20] recently have also stated and shown that additional frequency shifts appear in the subcortical gray matter, although they only suggest the possibility of chemical shifts and fast exchange processes as the sources. They then go on to refer to such shifts as “non-susceptibility contributions,” which

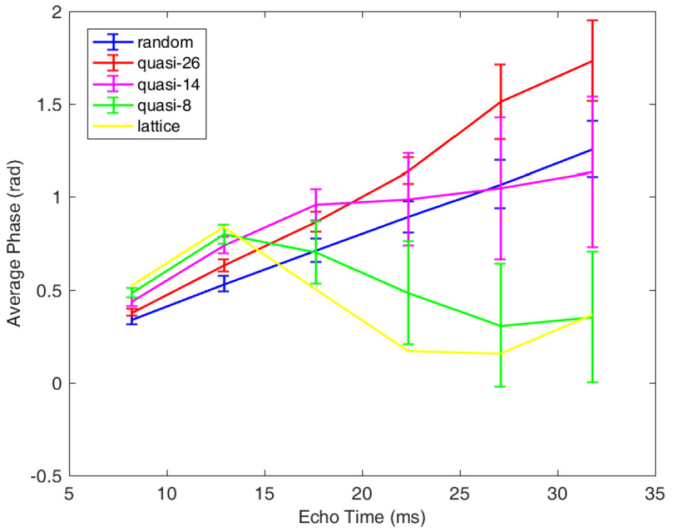

Fig. 6. Simulated phase values inside a cylinder perpendicular to the main field from different particle arrangements for a bulk susceptibility of − 0.24 ppm are shown as a function of echo time. Random particle arrangements, lattice, and quasi-random arrangements with each particle restricted within sub-volumes of 26^3, 14^3, and 8^3 grid points are simulated. Restricting particle arrangements leads to nonlinear phase dependence of echo time.

were actually found to be larger in the subcortical gray matter than in the white matter. A similar work by [19] had considered those additional frequency shifts only as chemical shifts. Thus, with a relatively small volume fraction of magnetic spherical particles, no one else has expected to see different phase shifts from spherical particles, with only a constant susceptibility value. Those "non-susceptibility" phase shifts determined from [20] or "chemical shifts" from [19] may still be from the susceptibility effect, as we have demonstrated here. Furthermore, the consequence of our work affects QSM methods, especially in the subcortical gray matter.

As the measured phase shown in Figs. 4 and 5 clearly deviates from Eq.(2), this fact strongly indicates that our experiments are not in the fast diffusion regime. For determining whether a particle is in the static dephasing or fast diffusion regime, we have considered two inequality

Table 2
R_2^* and R_2' (in units of Hz) of experimental and simulated data, respectively. The theoretical values calculated for the static dephasing regime are also included. For Fe_3O_4 nanoparticles, the values in the displayed columns from left to right correspond to highest bulk susceptibility to lowest.

Fe_3O_4	Experiment	Parallel	180 ± 42	135 ± 29	73 ± 13
		Perpendicular	201 ± 45	138 ± 26	74 ± 12
	Simulation	Parallel	318 ± 39	163 ± 14	90 ± 6
		Perpendicular	317 ± 39	162 ± 21	85 ± 7
	Theory	N/A	343	173	90
Polystyrene beads	Experiment	Parallel	54 ± 36		
		Perpendicular	57 ± 18		
	Simulation	Parallel	70 ± 10		
		Perpendicular	71 ± 11		
	Theory	N/A	74		

Table 3
Quantified $\Delta\chi'$ and R_2' from simulations using different particle arrangements. The more restricted arrangement of particles becomes, the larger R_2' becomes, while the quantified bulk susceptibility $\Delta\chi'$ from phase outside the cylinder is barely affected. This fact demonstrates the reliability of bulk susceptibility measurement from phase outside an object.

Arrangement	Sub-volume size	$\Delta\chi'$ (ppm)	R_2' (Hz)
Random	N/A	− 0.24 ± 0.01	71 ± 11
Quasi-random	26^3	− 0.24 ± 0.01	87 ± 12
Quasi-random	14^3	− 0.24 ± 0.01	118 ± 17
Quasi-random	8^3	− 0.25 ± 0.01	135 ± 19

formulas each given in [10,27]. With either formula, our bead experiments are in the static dephasing regime. On the other hand, as nanoparticles typically are smaller than 50 nm in diameter, with a field strength of 3 T, a susceptibility value of roughly $2 \cdot 10^5$ ppm, a diffusion constant of 2.5 μm^2/ms, and an echo time of 10 ms, either formula would predict the pure fast diffusion regime for nanoparticle solutions. As a result, one would expect no additional phase shifts inside the straws. This contradicts to our experimental results. This mismatch may

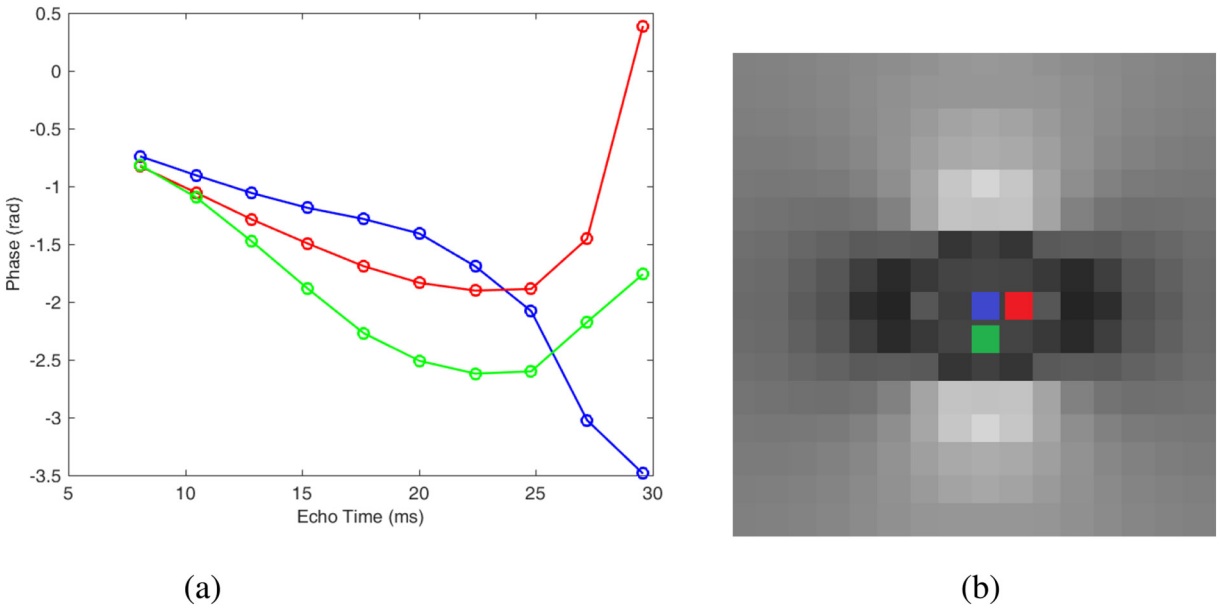

Fig. 7. (a) Phase values from three individual voxels inside an infinitely long cylinder perpendicular to the main field simulated for nanoparticles with a bulk susceptibility of 0.56 ppm. (b) The cross sectional plane of the simulated cylinder. Each color curve in (a) corresponds to the same color voxel in (b).

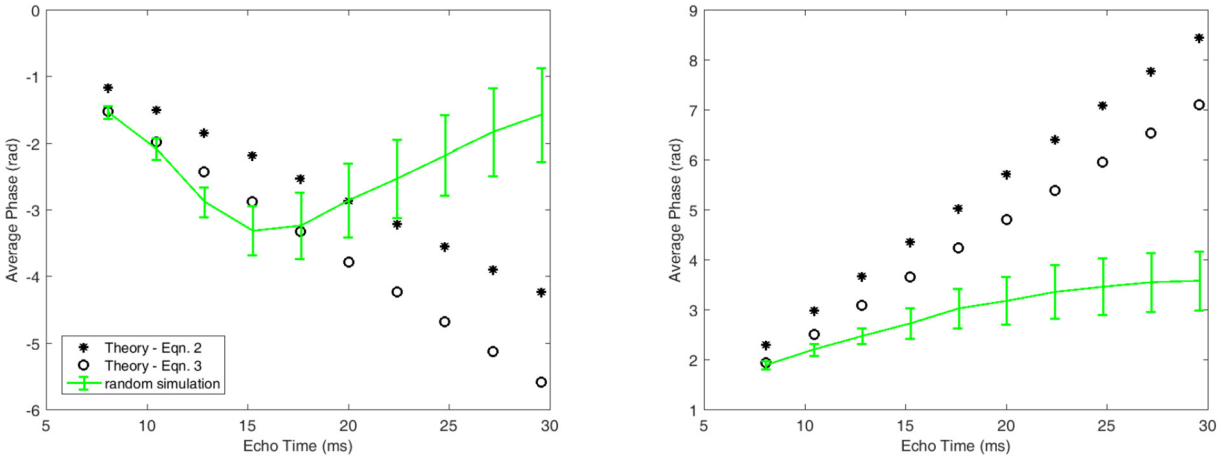

Fig. 8. (a) Phase values from inside an infinitely long cylinder perpendicular to the main field simulated for nanoparticles with a bulk susceptibility of 1.11 ppm. (b) Phase values from inside an infinitely long cylinder parallel to the main field simulated for the same nanoparticle solution. Both are extensions of the same simulations in Figs. 4c and 5c to longer echo times. As described in the text, these phase values were averaged from pixels inside the simulated cylinders. As a result, the Gibbs ringing effect has been heavily suppressed. Nonlinear phase over echo time is clearly seen in (a) and both simulated results do not agree with any theory at long echo times.

be explained by nanoparticle clustering. An effective nanoparticle size of around 120 nm [27] (or 270 nm [10]) in diameter would push the signals into the static dephasing regime. Additional phase shifts observed from some ferritin solutions in [12] also indicate clustering of ferritin to a diameter of at least 0.5 μm. However, in that study, some diffusion effects apparently mix with the static dephasing effect, as those observed phase shifts from ferritin solutions are much smaller than values estimated from Eq.(3) or our simulated results. This is also supported by the fact that the R_2^* measured from those ferritin solutions are much smaller than the R_2' estimated from simulations [12], as the diffusion effect will reduce R_2^* [28,29]. Furthermore, increased R_2 observed in tissues which contain ferritin compared to ferritin solutions has been attributed to clustering in tissues [30]. Histological staining for iron in the substantia nigra also indicates clustering of ferritin with diameters on the order of 10 μm [31] which would put it well into the static dephasing regime. All these results suggest that applications of QSM to iron quantification in the gray matter structure will likely lead to erroneous results, as QSM utilizes phase data both inside and outside objects. On the other hand, if only the phase outside an object is used for quantification, without being affected by the factors studied here, the magnetic moment of the object can be accurately quantified [15] and the bulk susceptibility of the object may also be accurately quantified with the known volume of the object.

The fact that nonlinear phase shifts varying over echo time can arise from only spherical particles with a constant susceptibility emphasizes the need for knowing details of ferritin arrangements in the subcortical gray matter, in addition to any other possible susceptibility sources. This fact also makes it difficult to establish a general theory, especially in the static dephasing regime that is considered in this work. Before introducing a new theory such as [21] or susceptibility anisotropy of a tissue or object [22,23], fields induced from discrete magnetic inclusions should be added first in the fashion of classical physics for the consideration of the additional phase shifts in tissues or objects containing ferritin.

5. Conclusion

We have shown that MRI phase signals inside long cylinders containing spherical particles with a constant susceptibility can vary nonlinearly with echo time. This fact, based on the principles of physics and MRI, is important to be taken into consideration, before other theories or susceptibility anisotropy is introduced for the revision of QSM, or before the problem is attributed to some biological effects. While only a simple model of discrete spheres within a cylinder is presented, it should be easy to see how these results could be extended to at least the subcortical gray matter which has more complicated geometries. The additional phase shifts, whether nonlinear or not, can affect in vivo QSM results. In addition, the fairly large uncertainties of R_2' from simulations may also explain the quantified human data as well. On the other hand, because of some confounding factors such as the arrangement of discrete particles (e.g., ferritin) and the Gibbs ringing effect inside an object, the magnetic moment of each individual object rather than QSM may be a more reliable and consistent quantification since only the phase outside the object is used.

Acknowledgments

This work was supported in part by the Department of Radiology at Wayne State University, President's Research Enhancement Award at Wayne State University, and grant support from DOD/USAMRAA W81XWH-12-1-0522. The content is solely the responsibility of the authors and does not necessarily represent the official views of the Department of Defense. We also acknowledge the use of the high performance computing Grid at Wayne State University. The authors would also like to thank the staff supports from Zahid Latif and Yang Xuan. The authors would also want to thank some materials and lab support from Prof. Matthew Allen and Prof. Bhanu Jena.

References

[1] Haacke EM, Cheng NY, House MJ, Liu Q, Neelavalli J, Ogg RJ, et al. Imaging iron stores in the brain using magnetic resonance imaging. Magn Reson Imaging 2005;23(1):1–25.
[2] Yi Wang, Tian Liu. Quantitative susceptibility mapping (QSM): decoding MRI data for a tissue magnetic biomarker. Magn Reson Med 2015;73(1):82–101.
[3] EMark Haacke, Saifeng Liu, Sagar Buch, Weili Zheng, Dongmei Wu, Ye Yongquan. Quantitative susceptibility mapping: current status and future directions. Magn Reson Imaging 2015;33(1):1–25.
[4] Wharton S, Bowtell R. Fiber orientation-dependent white matter contrast in gradient echo MRI. Proc Natl Acad Sci U S A 2012;109(45):18559–64.
[5] Duyn JH, Barbara TM. Sphere of Lorentz and demagnetization factors in white matter. Magn Reson Med 2014;72(1):1–3.
[6] Luo J, He X, Yablonskiy DA. Magnetic susceptibility induced white matter MR

signal frequency shifts-experimental comparison between Lorentzian sphere and generalized Lorentzian approaches. Magn Reson Med 2014;71(3):1251–63.
[7] JohnDavid Jackson. Classical Electrodynamics. John Wiley & Sons; 2012.
[8] Ruh A, Scherer H, Kiselev VG. The larmor frequency shift in magnetically heterogeneous media depends on their mesoscopic structure. Magn Reson Med 2018;79(2):1101–10.
[9] Durrant CJ, Hertzberg MP, Kuchel PW. Magnetic susceptibility: further insights into macroscopic and microscopic fields and the sphere of Lorentz. Concepts Magn Reson Part A 2003;18(1):72–95.
[10] Yablonskiy DA, Haacke EM. Theory of NMR signal behavior in magnetically inhomogeneous tissues: the static dephasing regime. Magn Reson Med 1994;32(6):749–63.
[11] Kokeny P, Cheng YN, Xie H. A study of MRI gradient echo signals from discrete magnetic particles with considerations of several parameters in simulations. Magn Reson Imaging 2018;48:129–37.
[12] He Xie, Cheng YuChungN, Paul Kokeny, Saifeng Liu, ChingYi Hsieh, EMark Haacke, et al. A quantitative study of susceptibility and additional frequency shift of three common materials in MRI. Magn Reson Med 2016;76(4):1263–9.
[13] Weisskoff Robert M, Suzanne Kiihne. MRI susceptometry: image-based measurement of absolute susceptibility of MR contrast agents and human blood. Magn Reson Med 1992;24(2):375–83.
[14] DWvan Krevelen. Properties of Polymers: Their Correlation with Chemical Structure, their Numerical Estimation and Prediction from Additive Group Contributions completely rev. 3rd Amsterdam; New York: Elsevier0444881603; 1990.
[15] He Xie, YuChungNorman Cheng, Saifeng Liu, Paul Kokeny. Removing unwanted background phase with a reference phantom for applications in susceptibility quantification. Magn Reson Imaging 2018;54:32–45.
[16] Xuancheng Shao, Johnson StevenG. Type-II/III DCT/DST algorithms with reduced number of arithmetic operations. Signal Process 2008;88(6):1553–64.
[17] Cheng YC, Hsieh CY, Neelavalli J, Haacke EM. Quantifying effective magnetic moments of narrow cylindrical objects in MRI. Phys Med Biol 2009;54(22):7025–44.
[18] Kokeny P, Cheng YN, Liu S, Xie H, Jiang Q. Quantifications of in vivo labeled stem cells based on measurements of magnetic moments. Magn Reson Imaging 2017;35:141–7.
[19] De Rochefort Ludovic, Ryan Brown, Prince MartinR, Wang YI. Quantitative MR susceptibility mapping using piece-wise constant regularized inversion of the magnetic field. Magn Reson Med An Official J Int Soc Magn Reson Med 2008;60(4):1003–9.
[20] Ferdinand Schweser, Robert Zivadinov. Quantitative susceptibility mapping (QSM) with an extended physical model for MRI frequency contrast in the brain: a proof-of-concept of quantitative susceptibility and residual (quasar) mapping. NMR Biomed 2018:e3999.
[21] He X, Yablonskiy DA. Biophysical mechanisms of phase contrast in gradient echo MRI. Proc Natl Acad Sci U S A 2009;106(32):13558–63.
[22] Chunlei Liu. Susceptibility tensor imaging. Magn Reson Med An Official J Int Soc Magn Reson Med 2010;63(6):1471–7.
[23] Cronin MatthewJ, Richard Bowtell. Quantifying MRI frequency shifts due to structures with anisotropic magnetic susceptibility using pyrolytic graphite sheet. Sci Rep 2018;8(1):6259.
[24] Duyn JeffH. Studying brain microstructure with magnetic susceptibility contrast at high-field. Neuroimage 2018;168:152–61.
[25] Duyn JeffH, John Schenck. Contributions to magnetic susceptibility of brain tissue. NMR Biomed 2017;30(4):e3546.
[26] Rudko DA, Klassen LM, de Chickera SN, Gati JS, Dekaban GA, Menon RS. Origins of r2* orientation dependence in gray and white matter. Proc Natl Acad Sci U S A 2014;111(1):E159–67.
[27] Kiselev VG, Novikov DS. Transverse NMR relaxation in biological tissues. Neuroimage 2018: https://doi.org/10.1016/j.neuroimage.2018.06.002.
[28] Muller RN, Gillis P, Moiny F, Roch A. Transverse relaxivity of particulate MRI contrast media: from theories to experiments. Magn Reson Med 1991;22(2):178–82. discussion 195-6.
[29] Weisskoff RM, Zuo CS, Boxerman JL, Rosen BR. Microscopic susceptibility variation and transverse relaxation: theory and experiment. Magn Reson Med 1994;31(6):601–10.
[30] Yves Gossuin, Pierre Gillis, Muller RobertN, Aline Hocq. Relaxation by clustered ferritin: a model for ferritin-induced relaxation in vivo. NMR in Biomed Int J Devoted to the Dev Appl Magn Reson In vivo 2007;20(8):749–56.
[31] Brammerloh MD, Weigelt I, Arendt T, Gavriilidis F, Scherf N, Jankuhn S, et al. Iron-induced relaxation mechanisms in the human substantia nigra: toward quantifying iron load in dopaminergic neurons. Proc 26th Annu Meeting ISMRM. 2018. p. 0188.